Physics of Fluids

Aeroacoustic characteristics of slat finlets

Cite as: Phys. Fluids **33**, 097102 (2021); https://doi.org/10.1063/5.0061367
Submitted: 25 June 2021 • Accepted: 14 August 2021 • Published Online: 09 September 2021

Hasan Kamliya Jawahar, Syamir Alihan Showkat Ali and Mahdi Azarpeyvand

Physics of Fluids ARTICLE scitation.org/journal/phf

Aeroacoustic characteristics of slat finlets

Cite as: Phys. Fluids **33**, 097102 (2021); doi: 10.1063/5.0061367
Submitted: 25 June 2021 · Accepted: 14 August 2021 ·
Published Online: 9 September 2021

View Online Export Citation CrossMark

Hasan Kamliya Jawahar,[1,a)] Syamir Alihan Showkat Ali,[2,b)] and Mahdi Azarpeyvand[1,c)]

AFFILIATIONS

[1]Department of Aerospace Engineering, University of Bristol, Bristol BS8 1TR, United Kingdom
[2]Faculty of Mechanical Technology, University Malaysia Perlis (UniMAP), 02600 Arau, Perlis, Malaysia

[a)]Author to whom correspondence should be addressed: hasan.kj@bristol.ac.uk
[b)]Electronic mail: syamir@unimap.edu.my
[c)]Electronic mail: m.azarpeyvand@bristol.ac.uk

ABSTRACT

An experimental study was performed on a 30P30N three-element high-lift airfoil fitted with different types of slat finlets and its noise reduction capabilities were assessed. To develop a better understanding of the noise reduction mechanism, simultaneous measurements of the unsteady surface pressure were taken at various locations at the vicinity of the slat cove and at far-field locations. While there was a small reduction in far-field noise for the fundamental peak, the use of slat finlets showed a substantial reduction in surface pressure fluctuations. The reduction of vortex shedding energy by the slat finlets also resulted in the reduction of nonpropagating hydrodynamic field between the slat and the main-element substantially reducing the near-field pressure spectra. Fourier and wavelet-based analysis along with high-order spectral analysis were provided for further confirmation of the observations and hypothesis. Finally, the wavelet coefficient findings showed spectral peaks as well as amplitudes modulated in time in the baseline case; however, these peaks were substantially reduced for the finlet configuration with larger spacing.

I. INTRODUCTION

The noise produced by aircraft engines has been greatly reduced since the invention and widespread use of engines with high bypass ratio; however, the noise created by the airframe has not changed. It is well known that during landing, high-lift devices and landing gears dominate the airframe noise. High-lift components, such as slats consisting of broadband and narrowband features in particular, contribute greatly to the airframe noise. Several passive and active flow control methods, such as morphing structures,[1–8] porous materials,[9–13] surface treatments,[14] serrations,[15–19] and transverse jets,[20,21] are being investigated to minimize the overall airframe noise. Despite this, the noise related to the conventional slat and wing configurations remains unresolved. Slat noise is primarily made up of broadband ($St_s = 0.5 - 1$) and narrowband ($St_s = 1 - 5$) components, where the slat-based Strouhal number is defined as $St_s = fc_s/U_\infty$, f is frequency, U_∞ is the freestream velocity, and c_s is the slat chord. Moreover, several studies have revealed many distinct tones for slat noise in the frequency range of $St_s = 1 - 5$[22–35] often only seen in small scales studies and are not so common in real flight conditions.

Aeroacoustic properties of slat noise have caught the attention of several researchers in recent years. Among the effective slat noise reduction mechanisms[36] is the slat cove cover,[37] slat hook extensions,[38] slat cove filler (SCF),[39–41] slat gap filler,[44] slat acoustic liners,[45] slat hook tripping,[46] slat hook serrations,[47] slat trailing-edge with porous treatments,[48,49] and slat wavy wall.[61] Among these slat noise treatments, one of the most effective methods is to fill the recirculation region within the slat cove in order to reduce the broadband noise produced by the slat.[39–41,50–58] The slat's tonal peaks are a product of a self-sustaining acoustic feedback loop resulting from the interaction between the unsteady shear layer of the slat cusp and the impingement on the lower surface of the slat, as described by Kamliya Jawahar *et al.*[41] Both the tonal noise and broadband noise produced by the shear layer impingement are removed by filling the slat cavity. To remove the unsteady recirculation area inside the slat cove, Horne *et al.*[39] placed a slat cove filler (SCF) on a Boeing 777–200 semi-span model using the slat cove filler profiles derived from a computational study. The results showed that a slat cove filler could reduce the broadband noise by up to 4–5 dB; however, this research did not provide any aerodynamic measurements.

Streett *et al.*[50] used a trapezoidal wing swept model to investigate the aerodynamic and noise reduction capabilities of the SCF configuration, demonstrating that noise is influenced by the angle of attack and the SCF configuration. The SCF had a significantly greater aerodynamic efficiency at $\theta < 20°$, with a 2° earlier stall. Regardless of its

noise reduction abilities, the high-lift airfoil's lift characteristics were susceptible to the SCF profile, according to Imamura *et al.*[53] and Ura *et al.*[54] Although the results indicated that noise reduction of up to 5 dB can be achieved for the SCF profiles, the lift characteristics remained unaffected. In addition, Tao and Sun[58] succeeded in optimizing the SCF profiles to maximize lift while reducing noise at a fixed angle of attack. Furthermore, in a recent experimental study, Kamliya Jawahar *et al.*[41] documented the effect of slat cove fillers on the aerodynamic and aeroacoustic performance of the high-lift airfoil. The results showed that slat cove fillers had no negative impact on the airfoil's aerodynamic behavior. Slat cove fillers further reduced the primary vortex shedding peak up to 3 and 10 dB in the broadband and narrowband regions, respectively. Recently, Kamliya Jawahar *et al.*[42] showcased a detailed study on the intermittent characteristics of slat tones revealing their dynamic characteristics. The study also revealed that the fundamental tone often observed as a spectral hump in slat noise does not only contain signatures of the Rossiter modes associated with the slat cusp shear flow instabilities but also possessed noise signatures arising from flow interactions with the main-element at the vicinity of the slat gap. Kopiev *et al.*[47] conducted a benchmark analysis using different slat serrations with various serration wavelengths. Serrations with shorter wavelengths were shown to be effective in reducing the far-field noise by up to 8 dB in the case of narrowband peaks. The results revealed that the slat serrations with a shorter wavelength had no effect on the aerodynamic performance and their use eliminated the characteristic narrowband peaks. Following that, in a recent study Kamliya Jawahar *et al.*[43] used two different types of slat cusp serrations for slat noise reduction. The study revealed that the aerodynamic characteristics of the high-lift devices remain unaffected by the use of both 2D and highly 3D slat cusp serrations. The use of 3D serrations were shown to better break the shear flow instabilities and the feedback mechanism that leads to slat tones, thus reducing the tone intensity and overall noise levels.

There is a significant gap in the literature when it comes to slat finlets. Clark *et al.*[59] investigated the utilization of finlets, or different surface treatments, for a tripped DU96-W180 airfoil to minimize the trailing-edge noise. The finlet treatments were mounted upstream of the trailing-edge in order to modify the boundary layer before reaching the trailing-edge. These treatments were found to be successful when compared to the untreated airfoil, offering up to 10 dB of broadband trailing-edge noise attenuation. Clark *et al.*[59] also investigated the effects of prolonging the finlet treatments exceeding the trailing-edge, concluding that finlets minimize the trailing-edge noise by changing the turbulence structures of the boundary layer at the vicinity of the trailing-edge. Furthermore, the treatment appeared to have a negligible aerodynamic effect. Their research, however, was restricted to noise measurements in the far-field, and physical phenomenon of the noise-control techniques was not adequately discussed.

Previous studies have shown that trailing-edge noise reduction can be achieved by the use of strategically placed finlets. The novelty of the present study is the use of finlets for slat noise reduction, which falls under the scope of cavity noise. This paper aims to present a comprehensive experimental analysis on the aeroacoustic characteristics of slat finlets with different spacings. Unsteady surface pressure measurements and far-field noise measurements are thoroughly analyzed to understand the aeroacoustic modification by the slat finlets. To better understand the slat finlets' noise reduction mechanism, Fourier analysis, coherence analysis, correlation analysis, higher spectral order analysis, and wavelet-based analysis coupled with stochastic analysis were used to advance the study.

II. EXPERIMENTAL METHODOLOGY

A. Wind tunnel and airfoil setup

Aeroacoustic tests were performed in the closed-circuit open-jet anechoic wind tunnel at the University of Bristol. The wind tunnel has a contraction ratio of 8.4:1 and a nozzle exit of 0.5×0.775 m^2. The anechoic wind tunnel can reach speeds up to 40 m/s and has a free-stream turbulence intensity of 0.25%.[60]

The 30P30N three-element high-lift airfoil used in the present study was built with a retracted chord length of $c = 0.35$ m and a span length of $l = 0.53$ m. In order to retain the flow's two-dimensionality within the slat and flap cove regions, the airfoil was designed without brackets within the test-section span. The slat was made using a spanwise slot to ease the installation of the interchangeable slat finlets. The airfoil model was tripped using a zigzag turbulator tape. The serrated trip has a thickness of about $h_t = 0.5$ mm, a width of $w_t = 3$ mm, and an angle of 70°. To ensure fully formed turbulence in the slat shear layer,[24] the trip was placed at $x/c = -0.055$ on the pressure side of the slat surface, upstream from the slat cusp. The x, y, and z axes in the Cartesian coordinates represent the streamwise, cross-wise, and spanwise directions, respectively. The 30P30N three-element high-lift airfoil schematic and the airfoil's geometrical parameters are presented in Fig. 1 and Table I, respectively. In the present study, the effects of slat finlet spacing were investigated using two different types of interchangeable slat finlet configurations with a self-thickness of 0.5 mm. Preliminary tests were carried out for a wide range of slat finlet spacings ($s = 4$, 8, 12, and 16 mm), and the results showed that finlet spacings larger than $s = 8$ mm did not modify the aeroacoustic characteristics of the slat for the tested high-lift configuration. Therefore, for the final tests presented here, the slat finlet spacings were chosen to be $s = 4$ and 8 mm. In the following sections, the slat finlet configurations will be referred to as finlet-1 ($s = 4$ mm) and finlet-2 ($s = 8$ mm), respectively. The general schematic of the slat finlet configuration used in the present study is provided in Fig. 2.

1. Acoustic measurements setup

A schematic diagram of the experimental setup with the 30P30N three-element high-lift airfoil placed in the anechoic chamber is shown

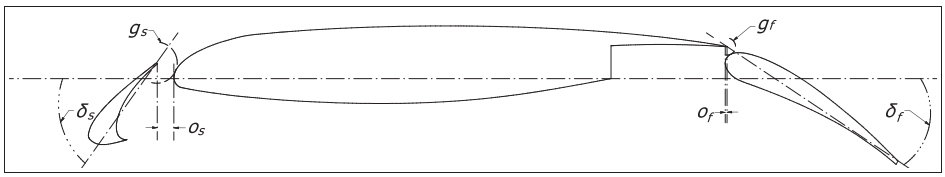

FIG. 1. Geometric parameters of the 30P30N three-element high-lift airfoil.

TABLE I. Geometrical parameters in percentage of retracted airfoil chord, $c = 0.35$ m.

Slat chord	c_s	$0.15c$
Main-element chord	c_{me}	$0.83c$
Flap chord	c_f	$0.3c$
Slat deflection angle	δ_s	30°
Flap deflection angle	δ_f	30°
Slat gap	g_s	2.95%
Flap gap	g_f	1.27%
Slat overhang	o_s	−2.5%
Flap overhang	o_f	0.25%

in Fig. 3. A Panasonic WM-61A electret microphone was used to test the far-field noise, positioned 1 m perpendicular from the slat trailing-edge. The microphone has a dynamic range of over 62 dB, with flat frequency response ranging from 50 Hz to 10 kHz. The far-field acoustic data were collected at a freestream velocity of $U_\infty = 30$ m/s, which corresponds to a chord-based Reynolds number of $Re_c = 7.0 \times 10^5$ ($Re_c = \rho U_\infty c/\mu$, where ρ is the density, U_∞ is the freestream velocity, c is the retracted high-lift airfoil chord, and μ is the dynamic viscosity of air). The measurements were performed at a sampling frequency of $f = 2^{15}$ Hz and for a sampling duration of 120 s. The results of the power spectrum were calculated by averaging the acquired data 220 times with a frequency resolution of $\Delta f = 2$ Hz. The excitation of the side frequencies was reduced by applying the Hanning window on the power spectral density. Sound pressure level (SPL) was calculated using $\mathrm{SPL} = 20 \cdot \log_{10}(p_{rms}/p_{ref})$, where p_{rms} refers to the acoustic pressure's root mean square and $p_{ref} = 20\,\mu$Pa represents the reference pressure. Acoustic pressure signal's sound pressure levels presented herein were corrected to a 1 m reference distance.

2. Unsteady surface pressure measurement setup

To measure the unsteady surface pressure in the slat cove region, electret condenser omnidirectional FG-23329-P07 pressure transducers (PTs) and remote sensors (RSs) were fitted over the slat and main-element of the 30P30N three-element high-lift airfoil, as shown in Fig. 4. The FG-23329-P07 pressure transducers are 2.5 mm in diameter and 2.5 mm in height, and circular sensing holes with a diameter of 0.8 mm were made on the main-element of the wing, as can be seen

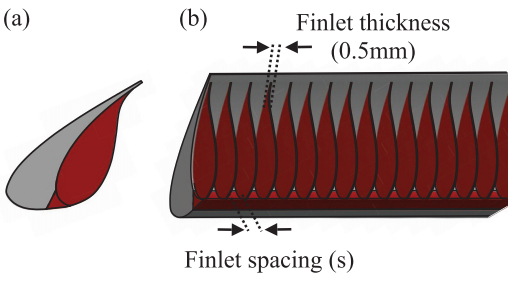

FIG. 2. Slat finlet schematic used in the present study: (a) side view and (b) geometrical parameters.

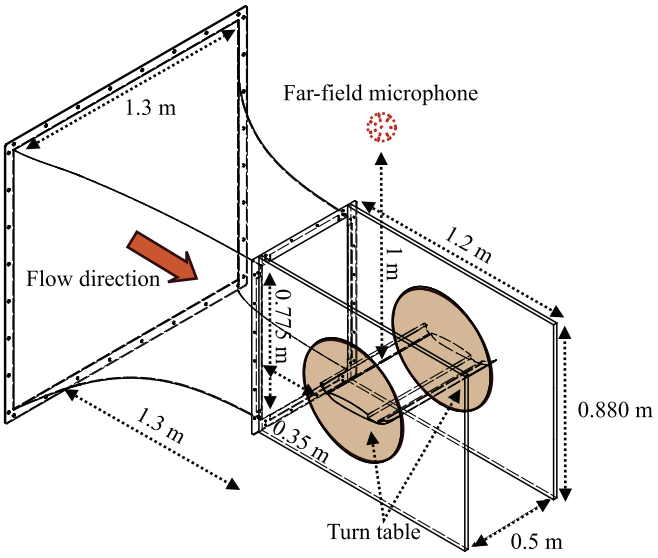

FIG. 3. Schematic of the experimental setup in the aeroacoustic wind tunnel.

in Fig. 5(a). In order to reduce attenuation errors at high frequencies because of the signal's spatial integration, a surface fairing made with a smaller sensing area of 0.4 mm was used [see Fig. 5(b)]. The transducers have a sensitivity of 22.4 mV/Pa in the flat frequency domain between 100 Hz and 10 kHz. The *in situ* calibration on the FG-transducers was done using a G.R.A.S 40PL microphone having an uncertainty level of ±1 dB in the current study. The sensitivity of the transducers was found to have a voltage range of 20.2–23.5 mV/Pa.

Additionally, the remote sensors developed using the Panasonic WM-61A miniature microphones were used within the slat cove region where there were space constraints to place the pressure transducers. The remote sensors were installed on the slat and the main-element of the wing, see Table II. They consist of a brass pipe fitted in a slot of a metal base holder as shown in Fig. 6. The microphone is installed in between the metal sections. The middle of the microphone's pinhole was connected with the center of another drilled pinhole attaching to the surface of the brass tubing. A flexible tube extension of 2 m was attached to one end of the brass pipe for anechoic termination to minimize the influence of standing waves. The remote sensors were calibrated *in situ* using the G.R.A.S 40PL piezoelectric microphone, which produced the transfer functions needed to compensate for high-frequency dissipation within the narrow tubes and the lag induced by the remote sensor extensions. The flat frequency

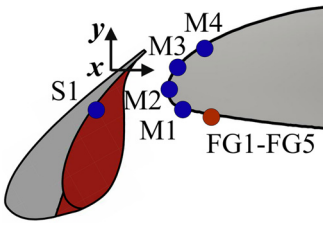

FIG. 4. The remote sensors (blue) and surface pressure transducers (red) locations on the slat and main-element of the 30P30N three-element high-lift airfoil.

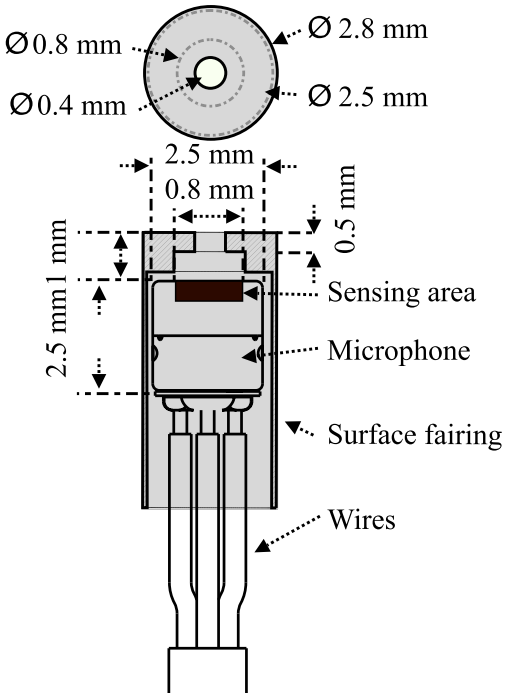

FIG. 5. Schematic view of the FG-23329-P07 pressure transducer fitted with the surface fairing.

response was found to have a range of up to 6 kHz ($St_s = 10$) for the current remote sensor configuration. It is important to note that all the near-field measurements using pressure transducers and remote sensors, and the far-field measurements were carried out simultaneously with a sampling frequency of $f = 2^{15}$ Hz for 120 s.

III. RESULTS AND DISCUSSION

A. Far-field spectral levels

Noise levels in the far-field were measured for the baseline, finlet-1, and finlet-2 configurations at a free-stream velocity of U_∞ = 30 m/s. The sound pressure level results measured using a far-field microphone at 1 m perpendicular from the slat trailing-edge at the angles of attack $\alpha = 14°$ and 18° are shown in Fig. 7. Sound pressure levels (SPL) are demonstrated as a function of slat-based Strouhal number ($St_s = f \times c_s/U_\infty$). Sound pressure levels for the baseline, finlet-1, and finlet-2 configurations have distinct narrowband peaks, especially at $St_s \approx 1.6$, which are typical in high-lift devices at geometric angles of attack $\alpha = 14°$ and 18°. In the case of finlet-1, there is a clear reduction in noise levels at $St_s \approx 1.6$ at the angle of attack $\alpha = 14°$ and 18°, but an increase in noise levels at $St_s \approx 2.3$ for the angle of attack $\alpha = 18°$. In contrast to the baseline and finlet-1 cases, there is a marginal decrease in noise at the fundamental peak ($St_s = 1.6$) for finlet-2 configuration at the angles of attack $\alpha = 14°$ and 18°. For both the finlet configurations, a small change in the peak frequency value to $St_s = 1.5$ and $St_s = 1.7$ (i.e., a lower and higher St_s number) is observed compared to the primary peak seen at $St_s = 1.6$ for the baseline configuration for both the presented angles of attack. Furthermore, for the finlet-1 and finlet-2 configurations, the SPL decreases from low- to mid-frequencies ($St_s < 2$) and remains constant at high frequencies ($St_s > 2$) at the angles of attack $\alpha = 14°$ and 18°. Particularly, a noticeable noise reduction can be seen at the spectral hump $St_s = 0.88$ at the angle of attack $\alpha = 18°$, with both finlet-1 and finlet-2 configurations exhibiting a decrease of up to 3 dB.

TABLE II. Streamwise (x axis) and spanwise (z axis) unsteady pressure measurement locations on the slat and main-element for the 30P30N three-element high-lift airfoil.

No.	Type[a]	x (mm)	y (mm)	z (mm)
S1	RS	−6.918	−11.622	265
M1	RS	17.347	−10.019	265
M2	RS	15.126	−5.839	265
M3	RS	17.622	0	265
M4	RS	23.520	5.485	265
FG1	PT	22.414	−11.356	277
FG2	PT	22.414	−11.356	280.6
FG3	PT	22.414	−11.356	288.4
FG4	PT	22.414	−11.356	301.4
FG5	PT	22.414	−11.356	319.6

[a]RS: remote sensor, PT: pressure transducer.

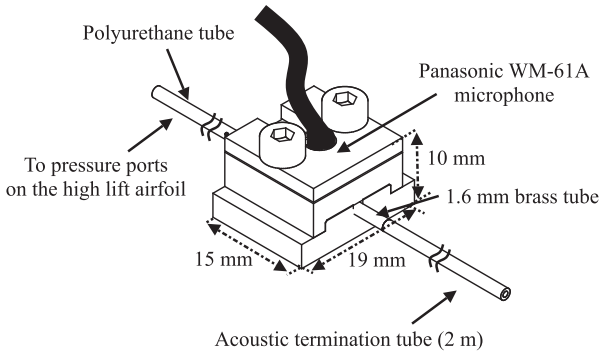

FIG. 6. Remote sensor configuration schematic view.

B. Near-field spectral levels

The effect of slat finlets and their noise generating mechanism was further investigated using the near-field unsteady pressure measurements. The surface pressure data were collected using pressure transducers and remote sensors on the surface of the slat (S1) and the main-element (FG1–FG5, M1–M4) of the airfoil at various streamwise and spanwise locations. The exact positions of the transducers are detailed in Table II.

The effects of the unsteady surface pressure measurements obtained by the pressure transducer FG1 at the leading-edge of the main-element are shown in Fig. 8. For the baseline case, the near-field noise spectra shows several distinct narrowband peaks with varying intensities for both the tested angles of attack, indicating the existence of cavity oscillation.[41] The results also clearly show the tonal peaks previously recorded in Fig. 7, especially the two dominant peaks at $St_s = 1.6$ and 3.2 for both angles of attack, as expected. Finlet-1 and finlet-2 configurations exhibit a

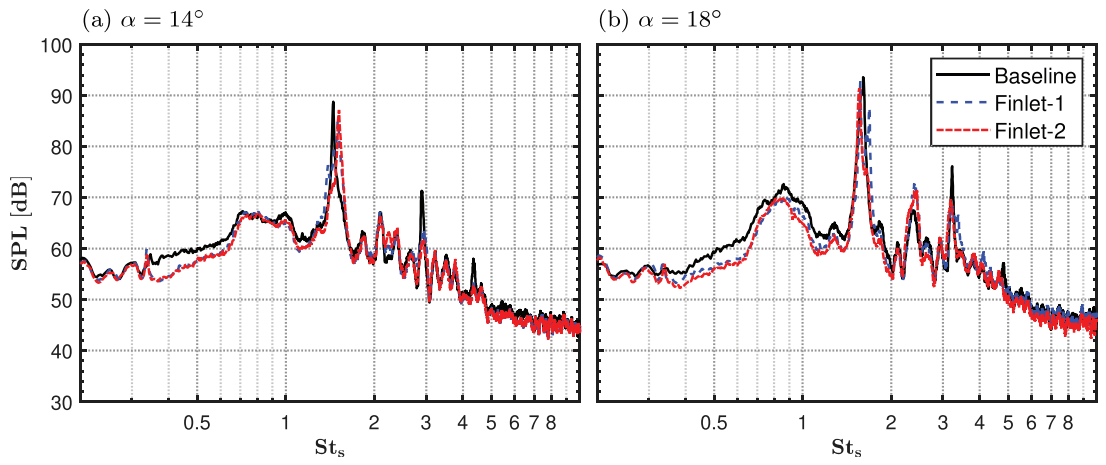

FIG. 7. Far-field noise spectra: (a) $\alpha = 14°$ and (b) $\alpha = 18°$.

similar pattern, with a marginal decrease in the surface pressure levels at the primary peak ($St_s = 1.7$) for the angle of attack $\alpha = 14°$. At the angle of attack $\alpha = 18°$, increased sound pressure levels can be observed for the peak frequency ($St_s = 1.7$) for the finlet-1 configuration and a significant reduction for finlet-2 compared to the baseline case. Moreover, the wall pressure spectra for the finlet-1 and finlet-2 configurations at the angle of attack $\alpha = 14°$ and $18°$ show decreased SPL over the entire frequency range, especially in the low-mid-frequencies ($St_s < 3$). The decreased spectral levels for the finlet-1 and finlet-2 configurations relative to the baseline in the near-field measurements can be observed in the far-field measurements in Fig. 7, indicating that the decreased spectra in the near-field have resulted from the propagating hydrodynamic energy field within the slat cove and the main-element. Additionally, the typical spectral hump ($St_s = 0.88$) generated from the slat noise was significantly reduced for the angle of attack $\alpha = 18°$ in the case of finlet-2. The reduction in the near-field spectra could be due to the spanwise energy distribution that arises from the compartmentalization of the spanwise flow structures by the use of finlets.

Figure 9 shows the unsteady surface pressure measurements at the slat and the leading-edge of the main-element obtained from the remote sensors. The results in Fig. 9 are presented only up to $St_s = 5.5$ considering the effect of the remote sensor's narrowband accuracy. In addition, the results from the far-field and unsteady surface pressure measurements observed in Figs. 7 and 8, respectively, show that the characteristic nature of slat tones lie within $St_s < 5.5$.

Generally, for all of the tested angles, the wall pressure fluctuation spectra exhibits multiple distinct narrowband peaks with different intensities at all the remote sensor locations, similar to the findings in Figs. 7 and 8. For all of the tested configurations, remote sensor S1, located in the slat area, has the lowest energy level compared to the other sensors (M1–M4) at the leading-edge of the main-element. At the angle of attack $\alpha = 14°$, the results of the slat wall pressure fluctuation spectra for finlet-1 and finlet-2 follow a similar pattern to the baseline but with slightly lower values at the fundamental peak ($St_s \approx 1.6$), as previously seen. The wall pressure fluctuations spectra at the leading-edge of the main-element for both the finlet cases reduce marginally over the entire frequency range, especially in the low-mid-

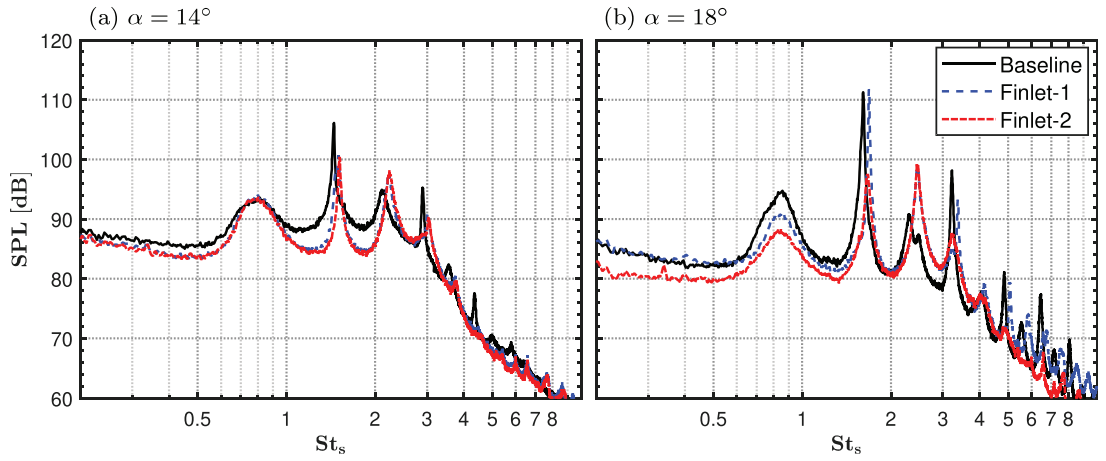

FIG. 8. Near-field spectra levels for the FG1 transducer on the main-element: (a) $\alpha = 14°$ and (b) $\alpha = 18°$.

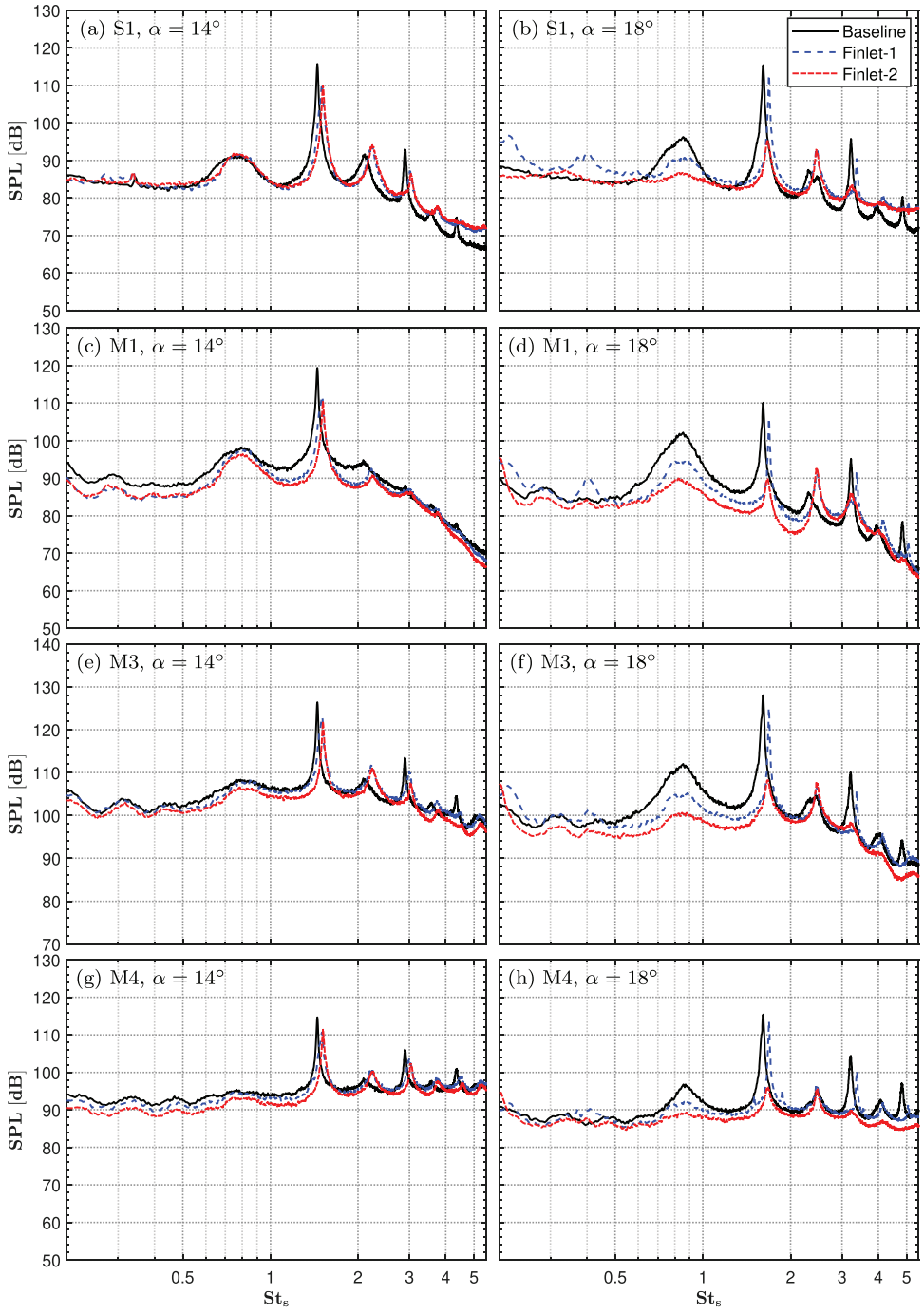

FIG. 9. Near-field surface pressure spectra for the remote sensor measurements: (a) S1, $\alpha = 14°$, (b) S1, $\alpha = 18°$, (c) M1, $\alpha = 14°$, (d) M1, $\alpha = 18°$, (e) M3, $\alpha = 14°$, (f) M3, $\alpha = 18°$, (g) M4, $\alpha = 14°$, and (h) M4, $\alpha = 18°$.

frequencies ($St_s < 3$). At the angle of attack $\alpha = 18°$, the results show that finlet-2 can significantly reduce the vortex shedding peak at $St_s = 1.6$ for all the presented measurement locations (S1, M1–M4). For both the finlet configurations, a slight shift in the peak Strouhal number to $St_s = 1.7$ (i.e., a higher St_s number) is observed compared to the narrowband peak seen at $St_s = 1.6$ for the baseline configuration for angles of attack $\alpha = 14°$ and 18°. Also, an increase in the noise levels at $St_s \approx 2.3$ can be seen with the use of finlet-1 and finlet-2 compared to the baseline case.

The appearance of the spectral hump ($St_s = 0.6 - 1$) in the case of the baseline, finlet-1, and finlet-2 at the angles of attack $\alpha = 14°$ and 18° is another notable feature shown in Fig. 9. The two finlet cases have a similar spectral hump pattern, with mildly reduced SPL at the leading-edge of the main-element (M1–M4) at

the angle of attack $\alpha = 14°$. At the angle of attack $\alpha = 18°$, the presence of the spectral hump is found to be more dominant. It is evident that the spectral hump is significantly suppressed for finlet-2 for all the presented sensor locations. In Fig. 7, the existence of the spectral hump is more prominent in the near-field surface pressure measurements than in the far-field measurements, suggesting the emergence of a nonpropagating hydrodynamic energy field within the slat and main-element. The emergence of the spectral hump ($St_s = 0.5 - 0.9$), seen in the baseline case, is believed be different in nature than that to the dominant even-numbered modes as shown by Kamliya Jawahar *et al.*[41]

1. Auto-correlation

An auto-correlation analysis of the unsteady surface pressure variations within the slat cove area can be used to evaluate the dominant time scales in the flow. The auto-correlation can be calculated using

$$R_{p_i p_i}(\tau) = \frac{\overline{p_i(t+\tau)p_i(t)}}{p^2_{i_{RMS}}}, \quad (1)$$

where p_i refers to the surface pressure, $p_{i_{RMS}}$ represents the surface pressure root-mean-squared, τ denotes the time delay, and the time average is depicted by the overbar.

Figure 10 shows the auto-correlation of the wall pressure fluctuations at the remote sensor locations S1 (slat) and M1 (main-element) for the baseline, finlet-1, and finlet-2 configurations at the angle of attack $\alpha = 14°$ and 18°. The results of the auto-correlation $R_{p_i p_j}(\tau)$ are plotted in response to the normalized time delay $\tau U_\infty / c_s$.

The $R_{p_i p_j}(\tau)$ results for the sensor on the slat (S1) show a slow decaying periodic behavior with a Gaussian curve for all the tested cases at both the angles of attack (14° and 18°), depicting the presence of a strong vortex shedding.[9,41] The interval between the two $R_{p_i p_j}(\tau)$ peaks in the baseline case shown in Fig. 10 equates to the vortex shedding frequency. The time delay observed for the baseline case in Fig. 10(a) is $\tau U_\infty / c_s \approx 0.625$, corresponding to the frequency of 914.28 Hz or $St_s = 1.6$, which is consistent with the primary peak shown in Figs. 8 and 9. At the angle of attack $\alpha = 18°$, the $R_{p_i p_j}(\tau)$ results for the finlet-2 case exhibit a very weak periodic shape with a quick decaying periodic behavior, suggesting the absence of a strong vortex shedding.

In the case of the sensor on the leading-edge of the main-element (M1), the $R_{p_i p_j}(\tau)$ results for all the tested cases show a slow decaying periodic behavior with a low decay rate at the angle of attack $\alpha = 14°$, fairly similar to the results observed in the slat location S1. The $R_{p_i p_j}(\tau)$ results for the finlet-1 and finlet-2 configurations at the angle of attack $\alpha = 18°$ display a very weak periodic form that decays instantly, suggesting the absence of a strong vortex shedding. The results reveal that the amplitude of the $R_{p_i p_j}(\tau)$ for the treated cases at the angle of attack $\alpha = 18°$ is much smaller than that of the results found at $\alpha = 14°$, demonstrating the suppression of vortex shedding energy in the region of the leading-edge of the main-element (M1). The absence of the strong vortex shedding for the finlet configurations

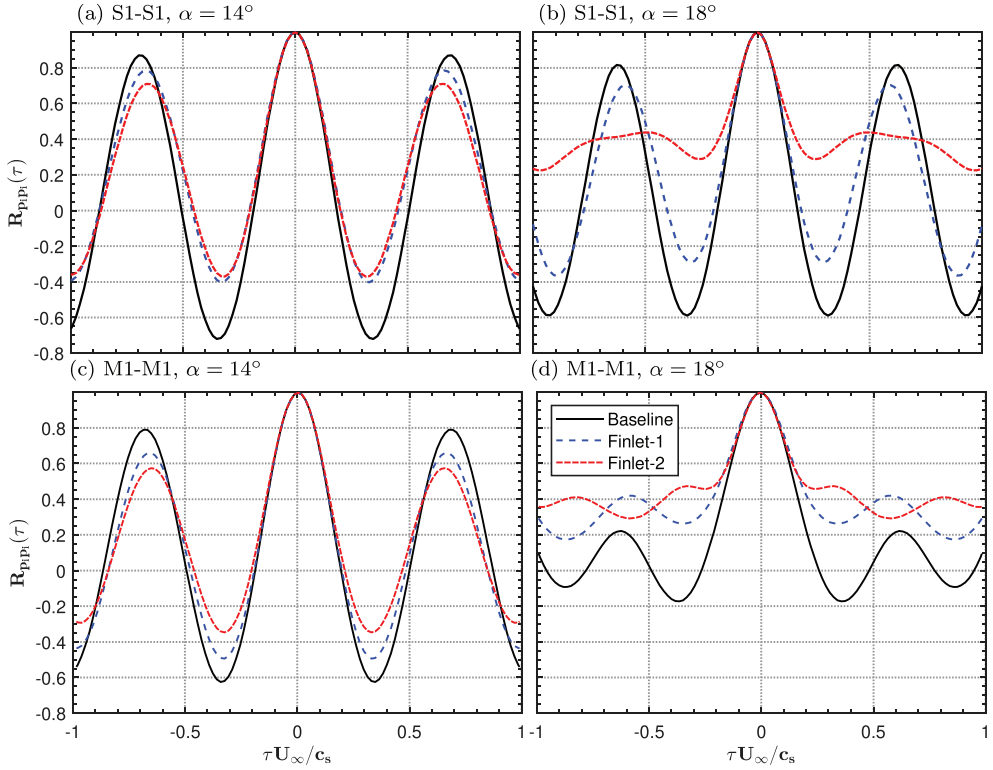

FIG. 10. Auto-correlation of the remote sensor at the locations S1 (slat) and M1 (main-element): (a) S1–S1, $\alpha = 14°$, (b) S1–S1, $\alpha = 18°$, (c) M1–M1, $\alpha = 14°$, and (d) M1–M1, $\alpha = 18°$.

could be attributed to the distribution of energy within small spanwise compartments by the use of finlets.

C. Coherence studies

Near-field coherence studies were performed to gain a deeper understanding of the flow structures' dynamics inside the slat and in the vicinity of the main-element leading-edge. The correlation between the phases of two separate remote sensors located in the streamwise and spanwise positions was measured over time, and the coherence of the signals can be determined from

$$\gamma^2_{p_i p_j}(f) = \frac{|\Phi_{p_i p_j}(f)|^2}{\Phi_{p_i p_i}(f)\Phi_{p_j p_j}(f)}, \tag{2}$$

where p_i is the reference sensor, while p_j is the second sensor used to measure the phase correlation with respect to the reference sensor. The remote sensor locations are detailed in Table II.

1. Cross-coherence

Figure 11 shows the coherence $\gamma^2_{p_i p_j}(f)$ between the reference transducer S1 on the slat and the other surface transducers M1–M4 on the leading-edge of the main-element for the three configurations (i.e., baseline, finlet-1, and finlet-2) at the angles of attack $\alpha = 14^\circ$ and $\alpha = 18^\circ$. The results generally represent high coherence between the pressure transducers S1 and M1 for all the three configurations at the angles of attack $\alpha = 14^\circ$ and $\alpha = 18^\circ$ over the entire frequency spectrum. The highest coherence levels occur at the tonal peaks, particularly at the fundamental vortex shedding peak ($St_s = 1.6$). High levels of coherence at the spectral hump ($St_s = 0.6$) can be observed for all the tested configurations. At the angle of attack $\alpha = 14^\circ$, the $\gamma^2_{p_i p_j}(f)$ finlet-1 and finlet-2 exhibit moderately lower coherence values at $St_s \approx 1.6$ compared to the baseline case. Furthermore, the baseline and finlet-2 cases have similar coherence values whereas

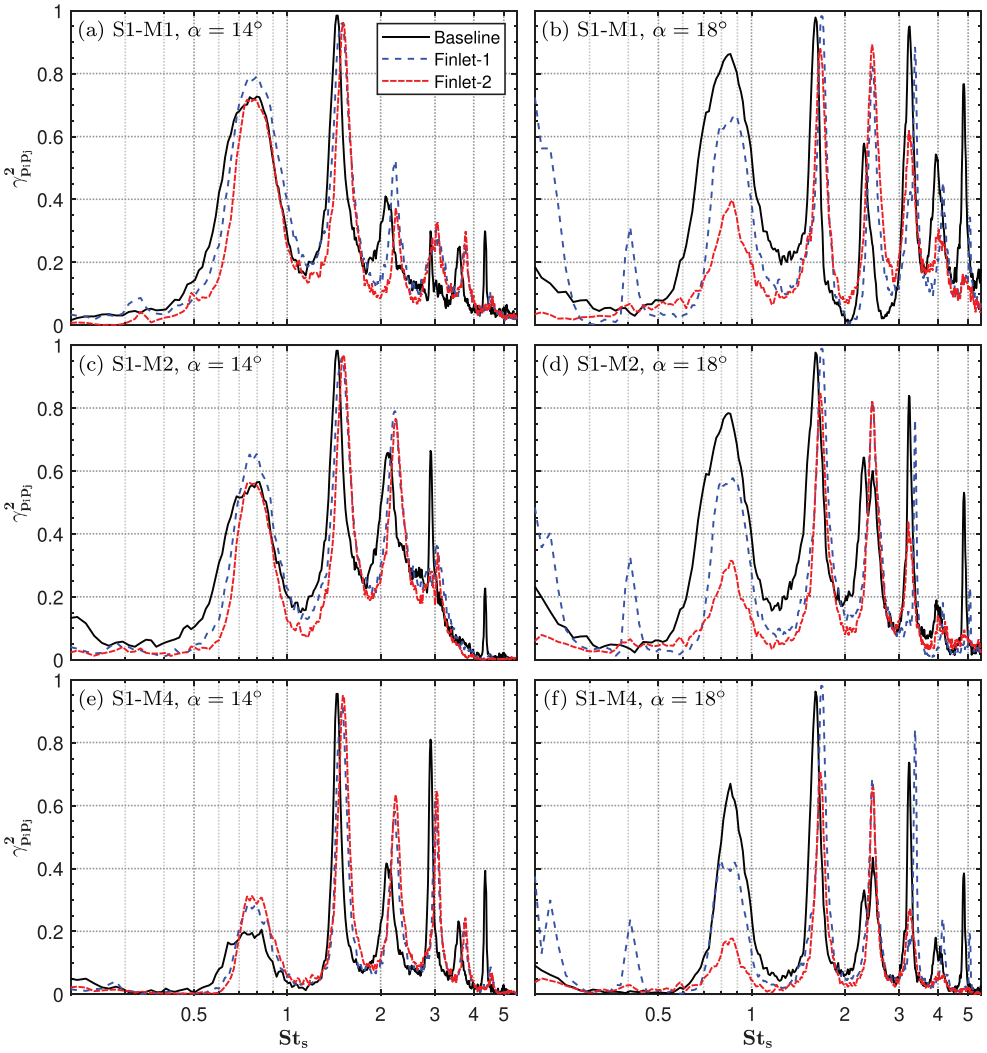

FIG. 11. Coherence between the remote sensors S1 on the slat and M1–M4 on the leading-edge of the main-element: (a) S1-M1, $\alpha = 14^\circ$, (b) S1-M1, $\alpha = 18^\circ$, (c) S1-M2, $\alpha = 14^\circ$, (d) S1-M2, $\alpha = 18^\circ$, (e) S1-M4, $\alpha = 14^\circ$, and (f) S1-M4, $\alpha = 18^\circ$.

larger near-field coherence values are observed in the case of finlet-1. At the angle of attack $\alpha = 18^{\circ}$, when compared to the baseline configuration, the $\gamma^2_{p_i p_j}(f)$ for the finlet-1 exhibits slightly higher coherence values at the vortex shedding peak ($St_s \approx 1.6$); however, as expected, lower coherence values at the fundamental peak are observed in the finlet-2 case. Additionally, for the broadband spectral hump and the tonal peaks, a significant reduction in $\gamma^2_{p_i p_j}(f)$ was observed for the finlet configurations, with finlet-2 portraying higher levels of reduction. Coherence results for all frequencies are almost zero for finlet-2 configuration, specifically for S1-M4. At the angle of attack $\alpha = 18^{\circ}$, the coherence results indicate that, except for tonal peaks, the three configurations have identical consistencies across the broadband spectrum, implying that they have similar three-dimensional flow structures. The coherence between the remote sensors located at the slat and leading-edge of the main-element with the finlet-2 configuration showed high levels of reduction relative to the other cases, in accordance with the near-field surface pressure spectra (see Fig. 8). In comparison with the baseline and finlet-1 cases, the coherence results for finlet-2 show a reduction in flow energy at all the transducer locations, particularly at the angle of attack $\alpha = 18^{\circ}$.

2. Spanwise coherence

The spanwise coherence results for the baseline, finlet-1, and finlet-2 configurations can theoretically enhance our knowledge of the flow structures and the pressure wave interference in the slat area and at the leading-edge of the main-element with and without the application of finlets. Figure 12 shows the spanwise coherence for the three configurations between the FG1 reference transducer and the FG2, FG3, and FG5 spanwise-located surface transducers. In the case of smallest lateral spacing $\Delta z/c_s$=0.07 (between FG1 and FG2), the $\gamma^2_{p_i p_j}(f)$ strong coherence

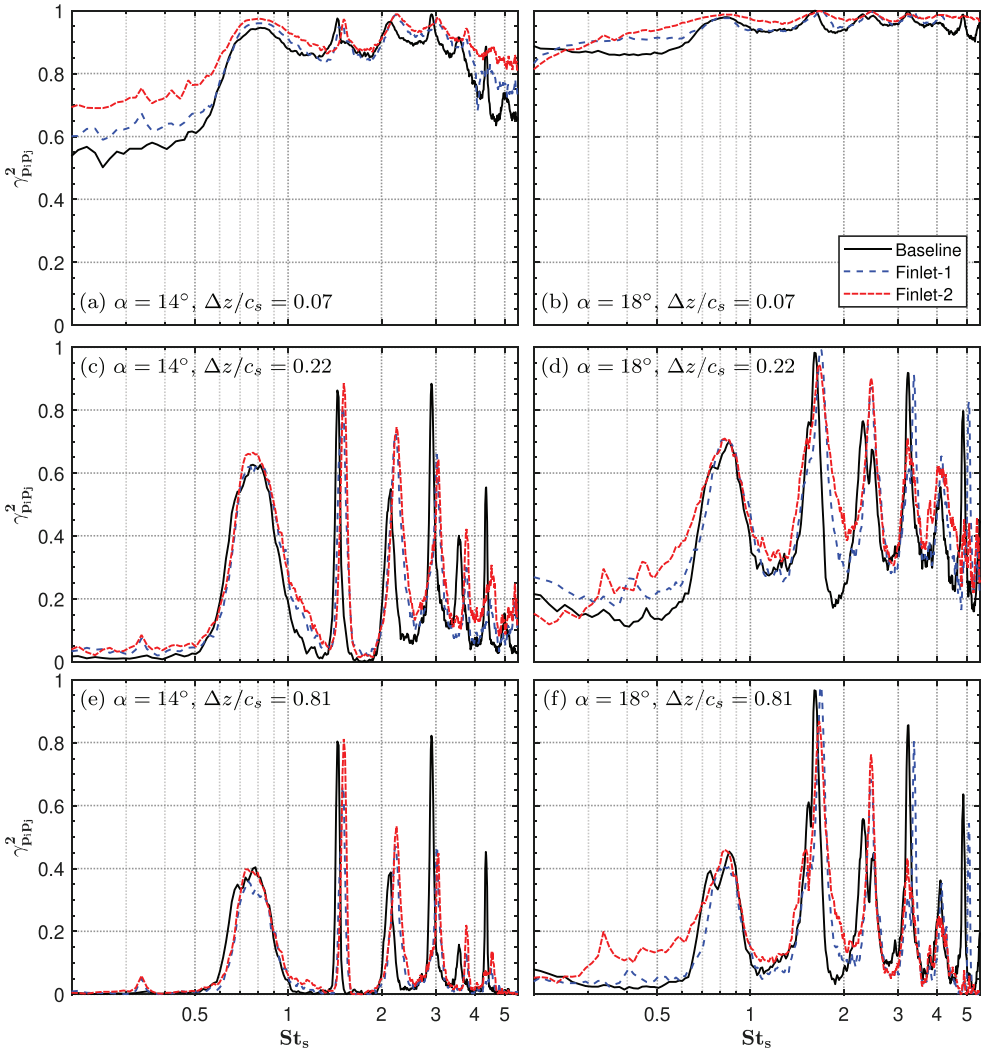

FIG. 12. Coherence between the spanwise surface pressure transducers on the main-element of the high-lift airfoil: (a) $\alpha = 14^{\circ}$, $\Delta z/c_s = 0.07$, (b) $\alpha = 18^{\circ}$, $\Delta z/c_s = 0.07$, (c) $\alpha = 14^{\circ}$, $\Delta z/c_s = 0.22$, (d) $\alpha = 18^{\circ}$, $\Delta z/c_s = 0.22$, (e) $\alpha = 14^{\circ}$, $\Delta z/c_s = 0.81$, and (f) $\alpha = 18^{\circ}$, $\Delta z/c_s = 0.81$.

for all the tested cases for the two angles of attack over the entire frequency spectrum can be observed. In the case of lateral spacing with $\Delta z/c_s = 0.22$ (between FG1 and FG3), the coherence results for the baseline and finlet cases [Fig. 12(c)] indicate a decrease in coherence in the broadband spectra but high levels of coherence at the tonal peaks. For the largest separation distance, $\Delta z/c_s = 0.81$ (between FG1 and FG5), the coherence for all the frequencies is nearly zero, except for the tonal peaks observed in the surface pressure spectra for both angles of attack. At the angle of attack $\alpha = 18°$, the three configurations have identical spanwise coherence over the broadband spectrum of the spectra (except for the tonal peaks), suggesting that all the cases exhibit three-dimensional flow structures. More importantly, the spectral hump at $St_s = 0.8$ reveals high degrees of coherence for all separation distances in the case of baseline, finlet-1, and finlet-2 configurations. It is worth noting that both the finlet-1 and finlet-2 configurations have high degrees of coherence at low frequencies (i.e., broadband spectral hump). This indicates that the spectral hump has a different source than the Rossiter modes as previously shown by Kamliya Jawahar *et al.*[41]

3. Spanwise correlation length scale

The noise produced in the vicinity of the slat via the interaction of pressure signals in the spanwise direction was investigated using the spanwise correlation length of wall pressure fluctuations. Using the spanwise coherence ($\gamma_{p_ip_j}$) results between the surface pressure transducers (FG1–FG5), the spanwise correlation length scale (Λ_γ) was calculated at different lateral spacing (Δz) using $\Lambda_\gamma(f) = \int_0^\infty \gamma_{p_ip_j}(f, \Delta z)\, d\Delta z$.

The correlation length scale (Λ_γ) for the baseline, finlet-1, and finlet-2 configurations at the angles of attack $\alpha = 14°$ and $18°$ is shown in Fig. 13. The Λ_γ results are presented as a function of Strouhal number (St_s). All of the cases were observed to follow a similar trend over the same length scales for both the angles of attack, except for tonal peaks at high frequencies ($St_s > 3$) for both the treated finlet-1 and finlet-2 cases where the tones were suppressed. For all cases at both angles of attack, the maximum length scale was observed at the fundamental tonal peak at about $\Lambda_\gamma/c_s = 0.082$. The length of the correlation scales over the entire frequency spectrum is greater for all of the tested configurations at the angle of attack $\alpha = 18°$ compared to that of $\alpha = 14°$. Furthermore, at $\alpha = 18°$, the length scales for the baseline configuration show two discrete peaks at the broadband spectral hump, which are absent in the finlet configurations. The emergence of these two distinct peaks will be further explained in Subsection III C 4. As a whole, the correlation length in the spanwise direction reaffirms that the finlet-1 and finlet-2 dampen the slat cavity's acoustic feedback system, thus reducing the primary tonal behavior and its harmonics only at high frequencies.

4. Near-to-far-field coherence

To discern the nonpropagating hydrodynamic field and the noise radiated to the far-field, the measurements of near-field unsteady surface pressure fluctuations and far-field noise were made simultaneously. The following equation was used to measure the near-to-far-field coherence:

$$\gamma^2_{p_ip_j}(f) = \frac{|\Phi_{p_ip_j}(f)|^2}{\Phi_{p_ip_i}(f)\Phi_{p_jp_j}(f)} \quad \text{for } p_i = \text{S1, M1 and } p_j = \text{FF}^{90°}, \quad (3)$$

where the reference sensors are denoted by S1 (slat) and M1 (main-element), the $\text{FF}^{90°}$ is the far-field microphone at a distance of 1 m perpendicular from the slat trailing-edge, and the $\Phi_{p_jp_j}$ refers to the cross-spectral density between the two sensors p_i and p_j.

Figure 14 shows the coherence $\gamma^2_{p_ip_{90°}}$ between the far-field microphone ($\text{FF}^{90°}$) and the near-field remote sensors (S1, M1) for the baseline, finlet-1, and finlet-2 configurations at the angles of attack $\alpha = 14°$ and $18°$. High coherence levels were found at all tonal peaks as a consequence of cavity oscillations, in line with the recent study by Kamliya Jawahar *et al.*[41] For the angle of attack $\alpha = 14°$, S1-$\text{FF}^{90°}$ has slightly higher coherence levels across the entire frequency spectrum than M1-$\text{FF}^{90°}$ across all the measured configurations. Evidently, the broadband hump ($St_s = 0.5 - 0.9$), the vortex shedding peak ($St_s \approx 1.6$), and the other discrete narrowband peaks are slightly reduced for the finlet configurations, specifically for M1-$\text{FF}^{90°}$. For the angle of attack $\alpha = 18°$, finlet-1 has high coherence levels particularly at the vortex shedding peak ($St_s = 1.6$) with a slight shift to a higher frequency. As compared to the baseline and finlet-1 configurations, the near-to-far-field coherence ($\gamma^2_{p_ip_{90°}}$) at the broadband hump could

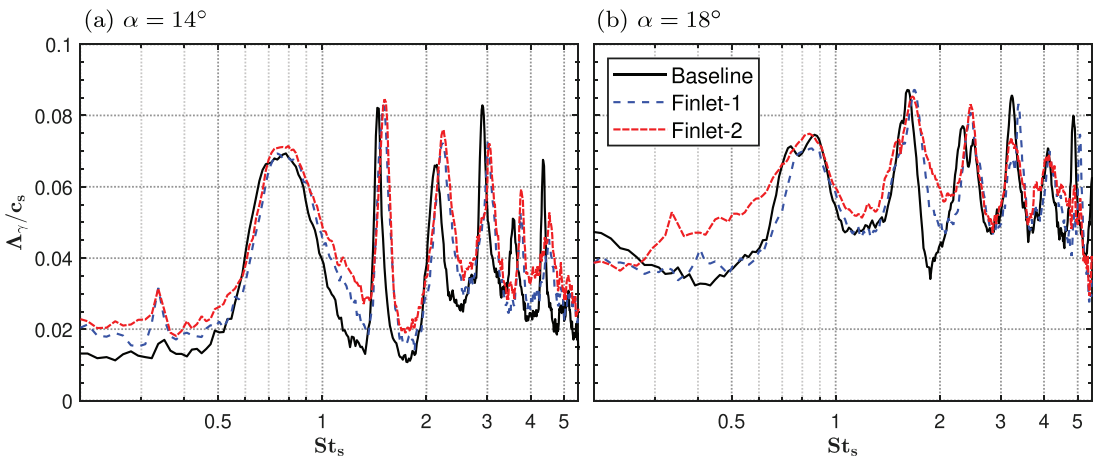

FIG. 13. Spanwise coherence length scales based on the spanwise coherence results: (a) $\alpha = 14°$ and (b) $\alpha = 18°$.

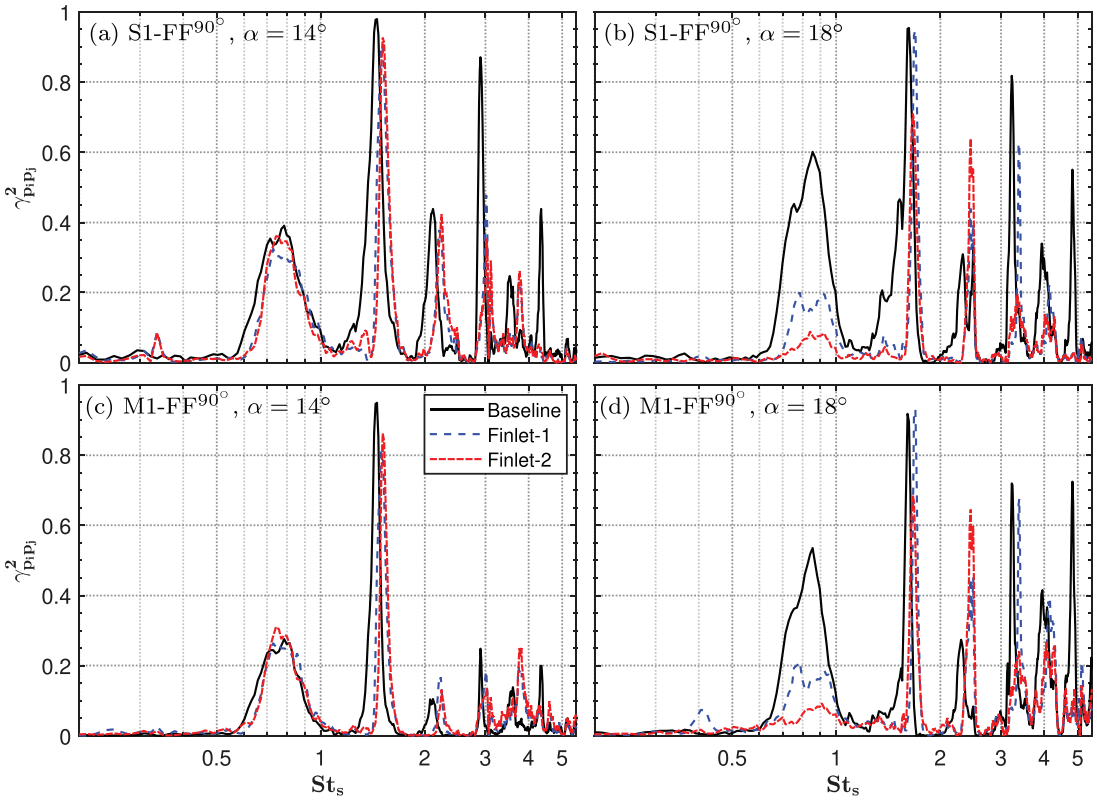

FIG. 14. Coherence between the near-field remote sensors S1 on the slat and M1 on the main-element with the far-field microphone 1 m away from the slat trailing-edge: (a) S1-FF$^{90^\circ}$, $\alpha = 14^\circ$, (b) S1-FF$^{90^\circ}$, $\alpha = 18^\circ$, (c) M1-FF$^{90^\circ}$, $\alpha = 14^\circ$, and (d) M1-FF$^{90^\circ}$, $\alpha = 18^\circ$.

be substantially reduced by using finlet-2 with the coherence values below $\gamma^2_{p_i p_{90^\circ}} < 0.1$. The reduced noise observed for the finlet-2 configuration in the near-field measurements, as seen earlier in Fig. 9, can be claimed merely as a result of the nonpropagating hydrodynamic field in the near-field most likely due to the effective compartmentalization of the spanwise flow structures within the slat cavity. Furthermore, for the slat with finlet configurations, the overall coherence of the spectral hump ($St_s = 0.5 - 0.9$) remains low, which is identical to the near-field pressure results (Fig. 9), especially at the angle of attack $\alpha = 18^\circ$, suggesting that the spectral hump is not caused by the hydrodynamic field inside the slat cavity and, therefore, is believed to be different in nature.[41,42]

D. Higher order spectral analysis

1. Normalized auto-bispectrum

Nonlinear energy transfer between the frequencies can be measured using the auto-bispectrum (B_{ppp})[41] to overcome the phase and quadratic coupling of the pressure signals with themselves. Auto-bispectrum will be normalized by its corresponding power spectrum components, known as the auto-bicoherence, which will be determined as follows:

$$b^2_{ppp}(f_i, f_j) = \frac{|B_{ppp}(f_i, f_j)|^2}{\Phi_{pp}(f_i + f_j)\Phi_{pp}(f_i)\Phi_{pp}(f_j)}. \quad (4)$$

Statistically independent frequency components (f_i, f_j and $f_i + f_j$) exhibit the auto-bicoherence of $b^2_{ppp} = 0$. If the frequency variable at $f_i + f_j$ shows some phase relationship with f_i and f_j, the auto-bicoherence is less than one (i.e., $0 < b^2_{ppp} < 1$), whereas when $b^2_{ppp} = 1$, perfect quadratic coupled waves are observed.

The auto-bicoherence contours for the surface pressure transducer FG1 on the leading-edge of the main-element for the baseline, finlet-1, and finlet-2 configurations at the angle of attack $\alpha = 18^\circ$ are shown in Fig. 15. It is worth noting that the mode numbers (St_{1-8}) correspond to the peaks found in the near-field surface pressure measurements in Fig. 8. The results for the baseline [Fig. 15(a)] show that the distinct peaks in Fig. 8(b) are induced by the modes in the slat cavity interacting with each other, i.e., the vortex shedding peak $St_s = 1.6$ [$St_{(2-2)}$], and the corresponding harmonics [$St_{(4-4)}$, $St_{(6-6)}$, $St_{(8-8)}$], leading to the formation of quadratic coupled modes.

The bicoherence value for the self-interacting modes at St_6 and St_8 is about $b^2_{ppp} > 0.8$, suggesting that these harmonics (i.e., $St_6 = 3St_2$ and $St_8 = 4St_2$) are generated by quadratic coupling.[41] The results show the probability of phase coupling between the even modes at $St_{2,4,6}$ with all other modes, except the odd modes, St_3, St_5, and St_7. For the spectral hump at St_1 ($St_s = 0.6$) shown in Fig. 8(b), self-interaction is absent, meaning the broadband hump is not quadratically coupled and is independent. In the case of finlet-1, the bicoherence contours exhibit a similar behavior to the baseline case, however, with a number of weak quadratic coupled modes, especially

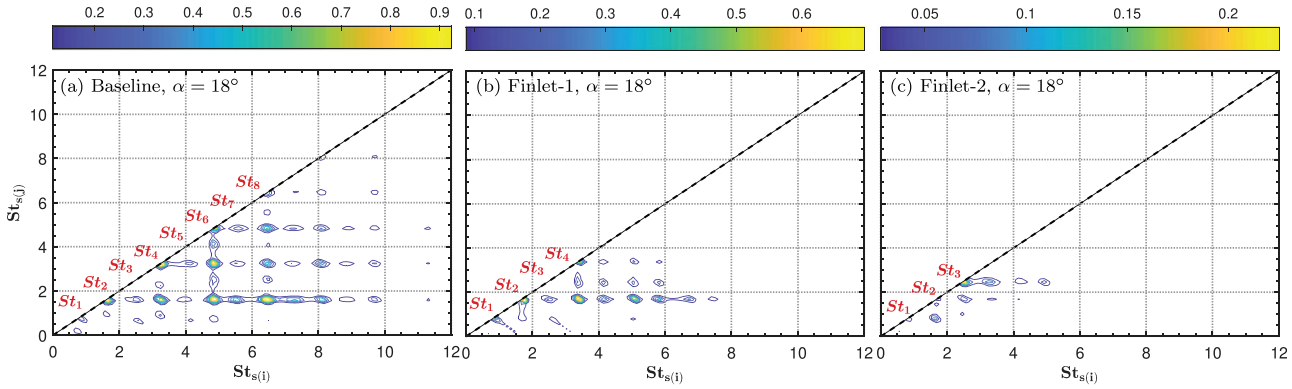

FIG. 15. The auto-bicoherence contours for the surface pressure transducer FG1 for (a) baseline, (b) finlet-1, and (c) finlet-2 configurations on the main-element at the angle of attack $\alpha = 18°$.

at the fundamental modes (St_2) and the other modes (i.e., St_4 and St_6), respectively. The slat configuration with finlet-2 exhibits similar results, albeit with weaker quadratic coupled modes, especially at the primary modes (St_2). They also demonstrate self-interaction with reduced bicoherence levels in the case of broadband hump, which is consistent with the findings shown in Fig. 8(b). As expected, at St_2, a weaker self-interaction appears, confirming that finlet-2 will substantially reduce the vortex shedding peak and the positive self-interaction of the modes is weakened when compared to the baseline case.

2. Persistence spectrum

The persistence spectrum or frequency spectrum was used to represent the signal's energy distribution over time as well as signal's phase coupling, which was used to further investigate the existence of the several distinct narrowband peaks shown in Fig. 8. The persistence range for the pressure signals acquired by the FG1 transducer was measured and presented in Fig. 16. The measurements were carried out for 120 s, and the time and frequency resolutions were 0.04 s and $St_s = 0.45$, respectively. The contour plots of the persistence spectrum were generated by superimposing several short-time Fourier transform (STFT) plots on top of each other. The persistence range for the baseline, finlet-1, and finlet-2 configurations at an angle of attack of $\alpha = 18°$ is shown in Fig. 16. The results indicate the existence of primary acoustic energy in the baseline and finlet-1 configurations, where the vortex shedding frequency ($St_s \approx 1.6$) and its harmonics have the highest energy content persisting over time. As can be seen from the contours, the highest energy content of the peaks are found to be densely spaced over time, with the tonal frequency (i.e., $St_s \approx 1.6$) demonstrating the ability to remain in a signal for the longest period of time. According to the auto-bicoherence results in Fig. 15, the odd St_s modes have significantly lower energy levels in the peak spread over time, indicating that there is no phase relationship between these modes and the even modes. The energy content was decreased in the finlet-2 configuration at $St_s \approx 1.6$ and its harmonics over time. The appearance of the spectral hump ($St_s = 0.6 - 1$) in Fig. 8(b) is not persistent in all conditions, but is well distributed in time. Consequently, the persistence spectrum results show that the application of finlet-2 reduces the characteristic slat flow features (i.e., the vortex shedding and the broadband spectral hump) as well as indicating that the flow is broadband and well distributed in time.

3. Wavelet analysis

Fourier and wavelet analyses are the well-known standard techniques for analyzing complex time signals. Fourier transforms are

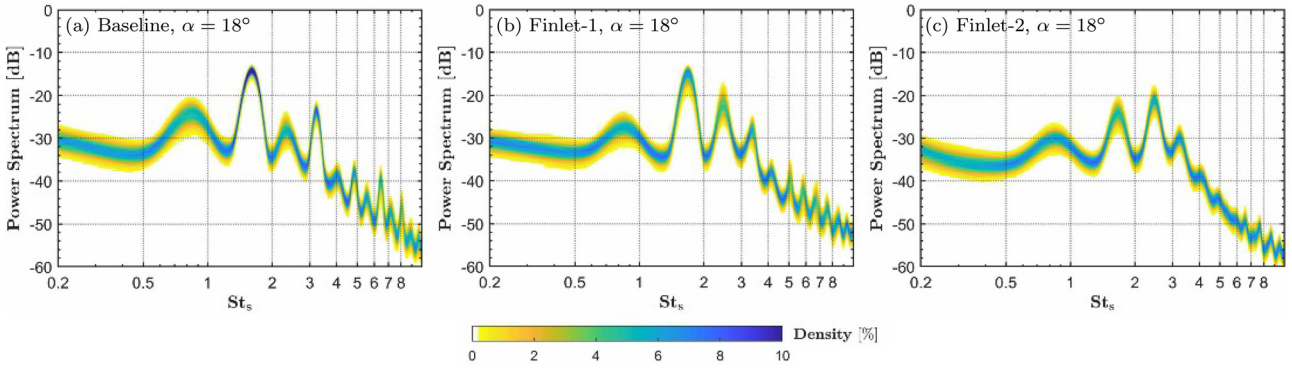

FIG. 16. The persistence spectrum contour for the surface pressure transducer FG1 for (a) baseline, (b) finlet-1, and (c) finlet-2 configurations on the main-element at angle of attack $\alpha = 18°$.

efficient in providing information on the dominant frequencies, whereas the wavelet analysis is well known for providing the time localization of the frequencies. However, the robustness of wavelet analysis is dependent upon the "mother" wavelet used to analyze the signal. Previous studies[64] have shown that the basic wavelet parameter k has a strong influence on the wavelet analysis. It is well established that the use of the Paul wavelet or smaller values of the wavelet parameter k provides a better time resolution, whereas the use of Morlet wavelet or a larger value of k improves the frequency resolution. Therefore, the choice of mother wavelet is dependent on the nature of the tested signal and the overall aim of the analysis. Since the present study focuses on the various broadband and narrowband frequencies that arise in slat noise and their stochastic characteristics, Morlet wavelet has been chosen as the mother wavelet for the present study.

a. Wavelet scalogram. The continuous wavelet transform (CWT) methodology was used in this study to analyze the temporal features of the pressure signals and their related frequencies. CWT was employed to analyze the amplitude modulation mechanisms associated with various narrowband peaks produced by the high-lift airfoils in the recent studies.[33,34,41] Farge[65] demonstrated that wavelet analysis can be used to classify the turbulence characteristics of a flow region. Continuous wavelet transform (CWT) is determined using the following formula:

$$W_x(a,\tau) = \frac{1}{\sqrt{C_\psi}} \int_{-\infty}^{+\infty} x(t)\, \psi^*_{a,\tau}\left(\frac{t-\tau}{a}\right) \mathrm{d}t, \tag{5}$$

where $W_x(a,\tau)$ refers to the CWT in terms of $x(t)$, $a > 0$ and a are the scale variable and the scale dilation parameter, respectively, τ is the time delay; the wavelet function is denoted by $\psi_{a,\tau}(t)$, $1/\sqrt{C_\psi}$ is a constant while $\psi^*\left(\frac{t-\tau}{a}\right)$ is the complex conjugate of the translated and dilated mother wavelet $\psi(t)$. The chosen Morlet kernel as the mother wavelet is also strongly supported by previous studies[41,62,63] for analyzing the complex time signal, and it is defined as $\psi(t) = \pi^{-1/4} e^{ikt} e^{-t^2/2}$, where k is the wavelet parameter, also known as the nondimensional frequency and is chosen to be 6.0 to satisfy the wavelet admissibility condition.[65] The CWT calculations were carried out for 120 s of the time signal, and the wavelet scalogram was presented for just 0.6 s outside the cone of influence for better visualization.

The wavelet coefficient modulus contour plots of the surface pressure signals at M3 on the leading-edge of the main-element for the baseline, finlet-1, and finlet-2 cases for $\alpha = 18^\circ$ are depicted in Fig. 17. Despite the fact that the wavelet analysis was performed on all of the remote sensor locations, the $W_x(a,\tau)$ results are only presented for the remote sensor M3 due to high levels of unsteady pressure loading in Fig. 8(f) and for the sake of brevity. The results for the baseline case indicate that the signal's temporal characteristics show amplitude modulation in time for the first three peaks in Fig. 8(b), suggesting that the amplitude of the modes are modulated over time. Furthermore, in the time–frequency domain, the fundamental peak at $St_s = 1.6$ is found to exhibit the most energy dominance. The slat configuration with finlet-1 reveals a similar pattern, with the fundamental vortex shedding peak moving to a higher frequency region at $St_s = 1.7$, as previously seen. The CWT is well distributed over the frequency region in the finlet-2 configuration, as anticipated, with lower peak or amplitude modulation. In contrast to the baseline case, finlet-2 contour reveals a vortex shedding peak with lower levels of energy and no other harmonic modes. Furthermore, the broadband hump has lower levels of energy and lesser occurrences as opposed to the tones.

b. Wavelet phase-space characteristics. Figure 18 shows the phase-space characteristics[65] of pressure fluctuations as well as the real part of the wavelet coefficients using the remote sensor M3. The real part of the wavelet coefficients is shown in Figs. 18(a)–18(c), while the phase-space characteristics are presented in Figs. 18(d)–18(f). The results in Fig. 18 are shown for a time span of 0.33 s for better phase-space characteristics visualization. All the three configurations clearly display distinct phase-space features, which can be divided into repetitive and cone-like patterns that could be evaluated accordingly. For the baseline configuration, both the real part and the phase-space of the wavelet coefficients show several repeated patches at St_2. The horizontal length of these patches, according to Farge,[65] corresponds to the spatial support of the flow structures, while the vertical length corresponds to the frequencies that characterize each excited wavepacket. The vortex shedding frequency is also associated with the phase-space activity at St_2 with repeated patches. At the broadband hump $St_s = 0.5 - 1$, the phase-space behavior shows energy density distributed in cone-like patterns, indicating the existence of coherent

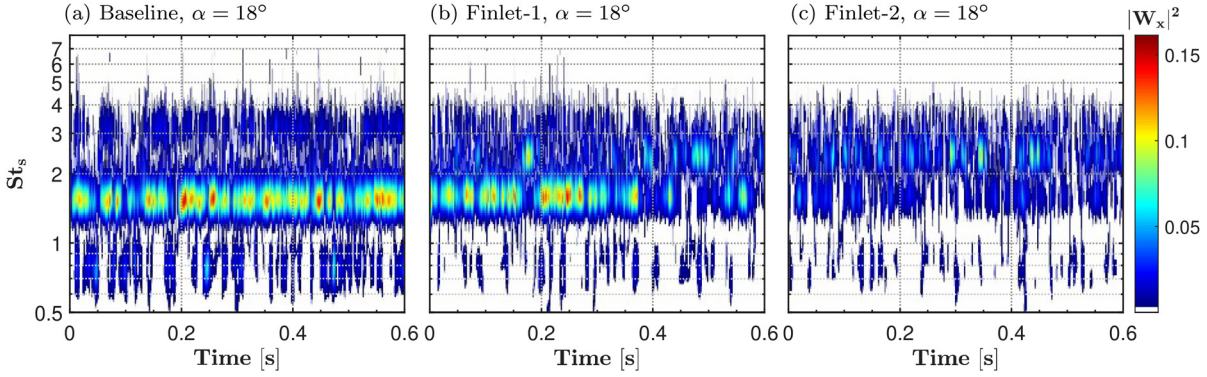

FIG. 17. Wavelet scalogram ($|W_x|$) for a segment of a pressure signal obtained at sensor location M3 at angle of attack $\alpha = 18^\circ$ for (a) baseline, (b) finlet-1, and (c) finlet-2 configurations.

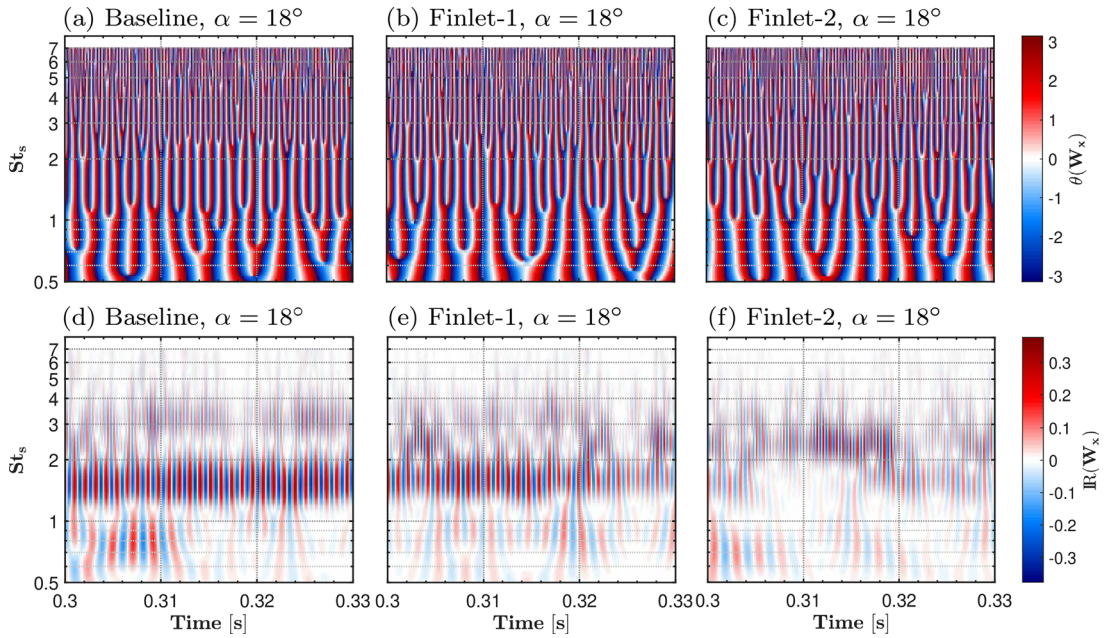

FIG. 18. The real part of the wavelet coefficient [(a) baseline, (b) finlet-1, and (c) finlet-2] and the phase-space characteristics [(d) baseline, (e) finlet-1, and (f) finlet-2] of the surface pressure fluctuations at M3 from the continuous wavelet transform.

structures with each cone pointing to an excited structure.[65] The spatial width of these cones at the broadband hump $St_s = 0.5$–1 is slightly greater than the repeated patches seen at St_2 reaffirming that the broadband hump at $St_s = 0.5 - 1$ is of a different nature. For the finlet-1 and finlet-2 cases, the results show that the energy is distributed in cone-like patterns of various sizes and bandwidths, indicating the existence of several coherent structures. The amplitude of the wavelet's real part for the finlet-2 configuration further indicates that these coherent structures have less energy than the baseline configuration.

c. Stochastic analysis. Arithmetic mean, standard deviation, and coefficient of variance of the wavelet coefficient modulus, i.e., $\mu(|W_x|)$, $\sigma(|W_x|)$, and CV $(|W_x|)$, respectively,[8] were used to examine the stochastic characteristics of the surface pressure fluctuation for the various frequencies of interest. Figure 19 presents the stochastic analysis of the wavelet coefficient modulus from remote sensors at the slat (S1) and the leading-edge of the main-element (M1–M4) for the baseline, finlet-1, and finlet-2 configurations at the angles of attack $\alpha = 18°$.

For the baseline and finlet-1 cases [Figs. 19(a) and 19(b)], increased values of $\mu(|W_x|)$ at M3 are observed along with a peak at $St_s = 1.6$. Sensor M3 has the highest fluctuation compared to the other sensor locations, despite the fact that all remote sensors have recorded this primary peak. Furthermore, the broadband hump at $St_s = 0.5 - 1$ indicates higher $\mu(|W_x|)$ levels at M3 when compared to other locations. The finlet-2 configuration [Fig. 19(c)] shows two peaks at $St_s = 1.6$ and $St_s = 2.3$ for the M3 remote sensor location, which are absent from the other remote sensor locations. The findings also show a significant reduction in $\mu(|W_x|)$ at the vortex shedding frequency ($St_s = 1.6$).

The degree of distribution of pressure events from the mean at a given frequency is indicated by the $\sigma(|W_x|)$. The baseline case shows two significant peaks in $\sigma(|W_x|)$ for the M2 and M3 remote sensor positions, respectively, at $St_s = 0.8$ and $St_s = 1.6$, which are aligned with the broadband hump spectra and the fundamental vortex shedding frequency. The peaks at the broadband hump ($St_s = 0.8$) indicate that the pressure variations at M2 and M3 are distributed away from the mean distribution with M3 having comparatively higher values. Finlet-2 exhibits a similar pattern, with two peaks at $St_s = 1.6$ and $St_s = 2.3$ for the M3 remote sensor, which is compatible with the $\mu(|W_x|)$ findings in Fig. 19(c). In contrast to the baseline and finlet-2 configurations, the $\sigma(|W_x|)$ for the finlet-1 configuration displays no distinct behavior but follows the same patterns as the $\mu(|W_x|)$.

The coefficient of variation CV$(|W_x|)$ is the standard deviation to mean ratio, which indicates the pressure signal fluctuation amplitude at a given frequency in terms of percentage.[66] The greater the dispersion around the mean, the higher the CV$(|W_x|)$. For the baseline, the CV$(|W_x|)$ clearly shows that $St_s = 0.8$ with higher values, i.e., up to 65%, is of a different type than $St_s = 1.6$ with lower values (up to 20%) for all slat and main-element locations. In contrast to the other sensors, the CV$(|W_x|)$ at M4 is poor at $St_s = 0.8$. The changes in CV$(|W_x|)$ remains low in the finlet-1 configuration for all frequencies and remote sensor locations, except for S1 at frequencies $St_s > 5$. When compared to the baseline and finlet-1 configurations, the variations in CV$(|W_x|)$ for the entire bandwidth at all locations are relatively low for the finlet-2 configuration. These findings confirm that the finlet application alters the flow structure within the slat region completely, and that the $St_s = 0.8$ and $St_s = 1.6$ are different in nature.

IV. CONCLUSION

Aeroacoustic performance of a three-element high-lift airfoil with and without slat finlets at the angles of attack $\alpha = 14°$ and 18° was investigated experimentally. The airfoil was equipped with

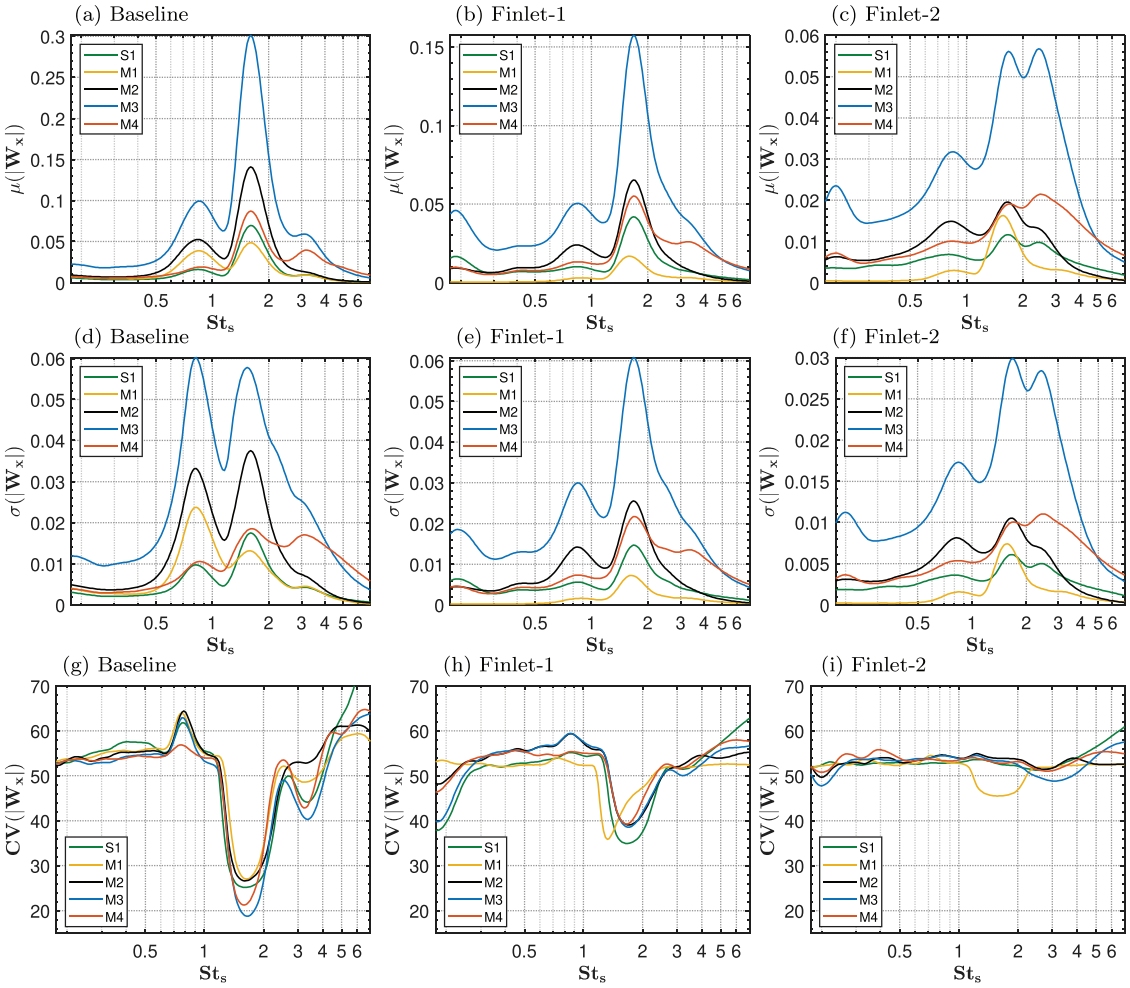

FIG. 19. Stochastic analysis for the various frequencies of interest: (a) baseline, $\mu(|W_x|)$, (b) finlet-1, $\mu(|W_x|)$, (c) finlet-2, $\mu(|W_x|)$, (d) baseline, $\sigma(|W_x|)$, (e) finlet-1, $\sigma(|W_x|)$, (f) finlet-2, $\sigma(|W_x|)$, (g) baseline, CV($|W_x|$), (h) finlet-1, CV($|W_x|$), and (i) finlet-2, CV($|W_x|$).

surfaces mounted unsteady surface pressure transducers around the slat and leading-edge of the airfoil's main-element. Although not presented here, a wide range of slat finlet spacings were tested and two finlet spacings with the best aeroacoustic performance were presented in this paper. It should be noted that finlets with larger spacing than that of the cases presented here do not show any noise modification compared to the baseline configuration. The slat noise's characteristic narrowband peaks were substantially reduced with the application of finlet-2 at the angle of attack $\alpha = 18°$ compared to the baseline and finlet-1, according to the near- and far-field surface pressure measurements. Furthermore, the finlet-2 configuration reduced the broadband hump seen in the baseline. When compared to the baseline case, the auto-correlation results of the finlet-2 demonstrated a very weak periodic shape with quick decaying periodic activity, meaning that the use of finlet-2 can significantly reduce the production of vortex shedding. The reduction in near-field energy for the finlet configurations could be attributed to the spanwise energy distribution that arises from the compartmentalization of the spanwise flow structures. Finlet-2 showed a substantial reduction of the broadband hump, the vortex shedding peak, and other distinct narrowband peaks when compared to the other tested configurations in the near-to-far-field coherence data. The wavelet coefficient results revealed spectral peaks in the baseline case as well as amplitudes modulated in time; however, these peaks were significantly reduced in the finlet-2 configuration. The results also revealed that the peaks observed in the baseline case have quadratic self-interaction in the slat cavity and the constructive self-interaction of the modes could be weakened using finlet-2. Finally, this paper shows that the application of finlet-2 reduces the tonal peaks thus the noise produced by the slat cavity. This research also demonstrated that finlets with right spacing could be used to break the feedback mechanism that drives the cavity-based oscillations.

ACKNOWLEDGMENTS

This research was sponsored by EU H2020 ARTEM project under the Grant Agreement ID 769359. We would like to

acknowledge Felix Gstrein for designing and manufacturing the 3D printed slat finlets.

DATA AVAILABILITY

The data that support the findings of this study are available from the corresponding author upon reasonable request.

REFERENCES

[1]H. Kamliya Jawahar, M. Azarpeyvand, and C. R. Ilario, "Aerodynamic and aeroacoustic performance of three-element high lift airfoil fitted with various cove fillers," AIAA Paper No. 2018-3142, 2018.

[2]H. Kamliya Jawahar, S. A. Showkat Ali, M. Azarpeyvand, and C. R. Ilario, "Aeroacoustic performance of three-element high lift airfoil with slat cove fillers," in *25th AIAA/CEAS Aeroacoustic Conference* (Delft University of Technology, Netherlands, 2019).

[3]H. Kamliya Jawahar, M. Azarpeyvand, and C. R. Ilario, "Experimental investigation of flow around three-element high-lift airfoil with morphing fillers," AIAA Paper No. 2017-3364, 2017.

[4]Q. Ai, H. Kamliya Jawahar, and M. Azarpeyvand, "Experimental investigation of aerodynamic performance of airfoils fitted with morphing trailing-edges," AIAA Paper No. 2016-1563, 2016.

[5]H. Kamliya Jawahar, Q. Ai, and M. Azarpeyvand, "Experimental and numerical investigation of aerodynamic performance of airfoils fitted with morphing trailing-edges," AIAA 2017-3371, 2017.

[6]H. Kamliya Jawahar, M. Azarpeyvand, and C. Silva, "Aerodynamic and aeroacoustic performance of airfoils fitted with morphing trailing-edges," AIAA Paper No. 2018-2815, 2018.

[7]H. Kamliya Jawahar, Q. Ai, and M. Azarpeyvand, "Experimental and numerical investigation of aerodynamic performance of airfoils with morphed trailing-edges," Renewable Energy **127**, 355–367 (2018).

[8]H. Kamliya Jawahar, M. Azarpeyvand, and C. R. I. da Silva, "Acoustic and flow characteristics of an airfoil fitted with morphed trailing-edges," Exp. Therm. Fluid Sci. **123**, 110287 (2021).

[9]S. A. Showkat Ali, M. Azarpeyvand, and C. Ilario, "Trailing-edge flow and noise control using porous treatments," J. Fluid Mech. **850**, 83–119 (2018).

[10]S. A. Showkat Ali, M. Szoke, M. Azarpeyvand, and C. Ilario, "Turbulent flow interaction with porous surfaces," AIAA Paper No. 2018-2801, 2018.

[11]S. A. Showkat Ali, M. Azarpeyvand, M. Szoke, and C. R. I. da Silva, "Boundary layer flow interaction with a permeable wall," Phys. Fluids **30**, 085111 (2018).

[12]S. A. Showkat Ali, M. Azarpeyvand, and C. R. I. da Silva, "Experimental study of porous treatment for aerodynamic and aeroacoustic purposes," AIAA Paper No. 2017-3358, 2017.

[13]S. A. Showkat Ali, M. Azarpeyvand, and C. R. I. da Silva, "Trailing-edge bluntness noise reduction using porous treatments," J. Sound Vib. **474**, 115257 (2020).

[14]A. Afshari, M. Azarpeyvand, A. A. Dehghan, and M. Szoke, "Trailing-edge noise reduction using novel surface treatments," AIAA Paper No. 2016-2834, 2016.

[15]X. Liu, H. Kamliya Jawahar, M. Azarpeyvand, and R. Theunissen, "Aerodynamic performance and wake development of airfoils with serrated trailing-edges," AIAA J. **55**(11), 3669–3680 (2017).

[16]Y. D. Mayer, B. Lyu, H. Kamliya Jawahar, and M. Azarpeyvand, "A semi-analytical noise prediction model for airfoils with serrated trailing-edges," Renewable Energy **143**, 679–691 (2019).

[17]S. H. S. Vemuri, X. Liu, B. Zang, and M. Azarpeyvand, "On the use of leading-edge serrations for noise control in a tandem airfoil configuration," Phys. Fluids **32**, 077102 (2020).

[18]X. Liu, S. A. Showkat Ali, and M. Azarpeyvand, "On the application of trailing-edge serrations for noise control from tandem airfoil configurations," AIAA Paper No. 2017-3716, 2017.

[19]E. Pang, A. Cambray, D. Rezgui, M. Azarpeyvand, and S. A. Showkat Ali, "Investigation towards a better understanding of noise generation from UAV propellers," AIAA Paper No. 2018-3450, 2018.

[20]M. Szoke, D. Fiscaletti, and M. Azarpeyvand, "Uniform flow injection into a turbulent boundary layer for trailing-edge noise reduction," Phys. Fluids **32**, 085104 (2020).

[21]M. Szoke, D. Fiscaletti, and M. Azarpeyvand, "Effect of inclined transverse jets on trailing-edge noise generation," Phys. Fluids **30**, 085110 (2018).

[22]M. Roger and S. Perennes, "Low-frequency noise source in two dimensional high-lift devices," AIAA Paper No. 2000-1972, 2000.

[23]A. Kolb, P. Faulhaber, R. Drobietz, and M. Grunewald, "Aeroacoustic wind turbine measurements on a 2D high-lift configuration," AIAA Paper No. 2007-3447, 2007.

[24]J. M. Mendoza, T. F. Brooks, and W. M. Humphreys, "An aeroacoustic study of a leading-edge slat configuration," Int. J. Aeroacoust. **1**(3), 241–274 (2002).

[25]S. Hein, T. Hohage, W. Koch, and J. Schoberl, "Acoustic resonances in a high-lift configuration," J. Fluid Mech. **582**, 179–202 (2007).

[26]M. Murayama, K. Nakakita, K. Yamamoto, H. Ura, and Y. Ito, "Experimental study of slat noise from 30P30N three-element high-lift airfoil in JAXA hard-wall low-speed wind tunnel," AIAA Paper No. 2014-2080, 2014.

[27]S. Makiya, A. Inasawa, and M. Asai, "Vortex shedding and noise radiation from a slat trailing-edge," AIAA J. **48**(2), 502–508 (2010).

[28]M. Terracol, E. Manoha, and B. Lemoine, "Investigation of the unsteady flow and noise generation in a slat cove," AIAA J. **54**(2), 469–489 (2016).

[29]C. C. Pagani, D. S. Souza, and M. F. Medeiros, "Slat noise: Aeroacoustic beamforming in closed-section wind tunnel with numerical comparison," AIAA J. **54**(7), 2100–2115 (2016).

[30]C. C. Pagani, D. S. Souza, and M. F. Medeiros, "Experimental investigation on the effect of slat geometrical configuration on aerodynamic noise," J. Sound Vib. **394**, 256–279 (2017).

[31]K. A. Pascioni and L. N. Cattafesta, "Unsteady characteristics of a slat-cove flow-field," Phys. Rev. Fluids **3**, 034607 (2018).

[32]L. Li, P. Liu, H. Guo, Y. Hou, X. Geng, and J. Wang, "Aeroacoustic measurement of 30P30N high-lift configuration in the test section with Kevlar cloth and perforated plate," Aerosp. Sci. Technol. **70**, 590–599 (2017).

[33]L. Li, P. Liu, H. Guo, X. Geng, Y. Hou, and J. Wang, "Aerodynamic and aeroacoustic experimental investigation of 30P30N high-lift configuration," Appl. Acoust. **132**, 43–48 (2018).

[34]L. Li, P. Liu, Y. Xing, and H. Guo, "Time-frequency analysis of acoustic signals from a high-lift configuration with two wavelet functions," Appl. Acoust. **129**, 155–160 (2018).

[35]L. Li, P. Liu, Y. Xing, and H. Guo, "Wavelet analysis of the far-field sound pressure signals generated from a high-lift configuration," AIAA J. **56**(1), 432–437 (2018).

[36]Y. Li, X. Wang, and D. Zhang, "Control strategies for aircraft airframe noise reduction," Chin. J. Aeronaut. **26**(2), 249–260 (2013).

[37]W. Dobrzynski, B. Gehlhar, and H. Buchholz, "Model and full scale high-lift wing wind tunnel experiments dedicated to airframe noise reduction," Aerosp. Sci. Technol. **5**(1), 27–33 (2001).

[38]M. R. Khorrami and D. P. Lockard, "Effects of geometric details on slat noise generation and propagation," Int. J. Aeroacoust. **9**(4–5), 655–678 (2010).

[39]W. C. Horne, K. D. James, T. K. Arledge, P. T. Soderman, M. Field, N. Burnside, and S. M. Jaeger, "Measurement of 26%-scale 777 airframe noise in the NASA Ames 40- by 80 foot wind tunnel," AIAA 2005-2810, 2005.

[40]H. Kamliya Jawahar, R. Theunissen, M. Azarpeyvand, and C. R. I. da Silva, "Flow characteristics of slat cove fillers," Aerosp. Sci. Technol. **100**, 105789 (2020).

[41]H. Kamliya Jawahar, S. A. Showkat Ali, M. Azarpeyvand, and C. Ilario, "Aerodynamic and aeroacoustic performance of high-lift airfoil fitted with slat cove fillers," J. Sound Vib. **479**, 115347 (2020).

[42]H. Kamliya Jawahar, S. Meloni, R. Camussi, and M. Azarpeyvand, "Intermittent and stochastic characteristics of slat tones," Phys. Fluids **33**(2), 025120 (2021).

[43]H. Kamliya Jawahar, S. A. Showkat Ali, and M. Azarpeyvand, "Serrated slat cusp for high-lift device noise reduction," Phys. Fluids **33**(1), 015107 (2021).

[44]T. L. Turner and D. L. Long, "Development of a SMA-based, slat-gap filler for airframe noise reduction," AIAA Paper No. 2015-0730, 2015.

[45]Z. Ma, M. Smith, S. Richards, and X. Zhang, "Slat noise attenuation using acoustic liner," in 11th AIAA/CEAS Aeroacoustics Conference (AIAA, 2005), p. 3009.

[46]W. Dobrzynski, K. Nagakura, B. Gehlhar, and A. Buschbaum, "Airframe noise studies on wings with deployed high-lift devices," in *4th AIAA/CEAS Aeroacoustics Conference* (AIAA, 1998), p. 2337.
[47]V. Kopiev, M. Zaitsev, I. Belyaev, and M. Mironov, "Noise reduction potential through slat hook serrations," in *17th AIAA/CEAS Aeroacoustics Conference (32nd AIAA Aeroacoustics Conference)* (AIAA, 2011), p. 2909.
[48]W. Dobrzynski, H. Bieler, L. C. Chow, and H. Remy, "The airframe noise reduction challenge: Lessons learned from the European Silencer Project," in Proposed Paper for DGLR Conference Deutscher Luft und Raumfahrt Kongress, Braunschweig (2006).
[49]M. Herr, "A noise reduction study on flow-permeable trailing-edges," in CD Proceedings ODAS (2007).
[50]C. Streett, J. Casper, D. Lockard, M. Khorrami, R. Stoker, R. Elkoby, W. Wenneman, and J. Underbrink, "Aerodynamic noise reduction for high-lift devices on a swept wing model," AIAA Paper No. 2006-212, 2006.
[51]C. Andreou, W. Graham, and H.-C. Shin, "Aeroacoustic study of airfoil leading-edge high-lift devices," AIAA Paper No. 2006-2515, 2006.
[52]C. Andreou, W. Graham, and H.-C. Shin, "Aeroacoustic comparison of airfoil leading-edge high-lift geometries and supports," AIAA Paper No. 2007-230, 2007.
[53]T. Imamura, H. Ura, Y. Yokokawa, S. Enomoto, K. Yamamoto, and T. Hirai, "Designing of slat cove filler as a noise reduction device for leading-edge slat," AIAA Paper No. 2007-3473, 2007.
[54]H. Ura, Y. Yokokawa, T. Imamura, T. Ito, and K. Yamamoto, "Investigation of airframe noise from high lift configuration model," AIAA Paper No. 2008-19, 2008.
[55]A. Shmilovich, Y. Yadlin, and D. M. Pitera, "Wing leading-edge concepts for noise reduction," in 27th International Congress of the Aeronautical Sciences (ICAS) (2010).
[56]A. Shmilovich and Y. Yadlin, "High-lift systems for enhanced take-off performance," in *28th International Congress of the Aeronautical Sciences* (International Congress of the Aeronautical Sciences, 2012), pp. 1–13.
[57]W. D. Scholten, D. J. Hartl, T. L. Turner, and R. T. Kidd, "Development and analysis-driven optimization of superelastic slat-cove fillers for airframe noise reduction," AIAA J. **54**, 1078–1094 (2015).
[58]J. Tao and G. Sun, "A novel optimization method for maintaining aerodynamic performances in noise reduction design," Aerosp. Sci. Technol. **43**, 415–422 (2015).
[59]I. Clark, N. Alexander, W. Devenport, S. Glegg, J. Jaworski, C. Daly, and N. Peake, "Bio-inspired trailing-edge noise control," AIAA J. **55**(3), 740–754 (2017).
[60]Y. Mayer, H. Kamliya Jawahar, S. Mate, S. A. Showkat Ali, and M. Azarpeyvand, "Design and performance of an aeroacoustic wind tunnel facility at the University of Bristol," Appl. Acoust. **155**, 358–370 (2019).
[61]G. Chen, X. Tang, X. Yang, P. Weng, and J. Ding, "Noise control for high-lift devices by slat wall treatment," Aerosp. Sci. Technol. **115**, 106820 (2021).
[62]S. Mallat, *A Wavelet Tour of Signal Processing* (Academic, New York, 1998).
[63]J. Morlet, "Sampling theory and wave propagation," in Proceedings of the 51st Annual Meeting of the Society Exploration Geophysics (1981).
[64]D. I. Moortel, S. A. Munday, and A. W. Hood, "Wavelet analysis: The effect of varying basic wavelet parameters," Sol. Phys. **222**(2), 203–228 (2004).
[65]M. Farge, "Wavelet transforms and their applications to turbulence," Annu. Rev. Fluid Mech. **24**(1), 395–458 (1992).
[66]P. S. Addison, *The Illustrated Wavelet Transform Handbook: Introductory Theory and Applications in Science, Engineering, Medicine and Finance* (CRC Press, 2017).